

---

# XTransfer: Modality-Agnostic Few-Shot Model Transfer for Human Sensing at the Edge

---

Yu Zhang<sup>1</sup> Xi Zhang<sup>1</sup> Hualin Zhou<sup>1</sup> Xinyuan Chen<sup>1</sup> Shang Gao<sup>1</sup> Hong Jia<sup>2</sup> Jianfei Yang<sup>3</sup> Yuankai Qi<sup>1</sup>  
Tao Gu<sup>1</sup>

## Abstract

Deep learning for human sensing on edge systems presents significant potential for smart applications. However, its training and development are hindered by the limited availability of sensor data and resource constraints of edge systems. While transferring pre-trained models to different sensing applications is promising, existing methods often require extensive sensor data and computational resources, resulting in high costs and limited transferability. In this paper, we propose XTransfer, a first-of-its-kind method enabling modality-agnostic, few-shot model transfer with resource-efficient design. XTransfer flexibly uses pre-trained models and transfers knowledge across different modalities by (i) *model repairing* that safely mitigates modality shift by adapting pre-trained layers with only few sensor data, and (ii) *layer recombining* that efficiently searches and recombines layers of interest from source models in a layer-wise manner to restructure models. We benchmark various baselines across diverse human sensing datasets spanning different modalities. The results show that XTransfer achieves state-of-the-art performance while significantly reducing the costs of sensor data collection, model training, and edge deployment.

## 1. Introduction

Human sensing refers to the process of capturing and interpreting data related to human activities, behaviors, and physiological states using various sensors (Zhang et al., 2023a). With the proliferation of edge devices equipped with sensors, human sensing plays a vital role in edge systems to understand contexts and enable smart applications,

---

<sup>1</sup>Macquarie University, Sydney, NSW, Australia <sup>2</sup>The University of Auckland, Auckland, New Zealand <sup>3</sup>Nanyang Technological University, Singapore. Correspondence to: Yu Zhang <y.zhang@mq.edu.au>, Tao Gu <tao.gu@mq.edu.au>.

ranging from activity recognition to emotion or vital sign detection (Ahamed & Farid, 2018). Deep learning (DL) offers robust performance in interpreting sensor data, and its deployment on edge devices improves privacy and reduces bandwidth (Zhang et al., 2020; Chen et al., 2020). However, existing DL solutions are often data- and resource-intensive for training and deployment (Dhar et al., 2021), posing significant challenges for data collection and edge deployment in human sensing (Sobin, 2020; Liu et al., 2019).

Unlike other data modalities (e.g., vision or text), collecting human sensing data for training can be costly and even impractical. This is uniquely due to the data that presents brittleness (i.e., noise sensitivity, low SNR), inconsistency (i.e., user variance, scenario changes), and heterogeneity (i.e., differences in hardware configuration) (Lane & Georgiev, 2015; Jeyakumar et al., 2019; Teh et al., 2020). Collecting such data typically requires ethical approvals, as it involves sensitive information (e.g., location, motion patterns) that raises privacy concerns (Zhang et al., 2022). Manual annotation of large volumes of sensor data is labor-intensive and incurs high costs (Song et al., 2023). Importantly, human sensing spans various modalities (e.g., IMU, ultrasound, mmWave radar) and data types (e.g., spectrograms, Doppler profiles, time series), further amplifying the costs of applying DL solutions and naturally leading to cross-modality scenarios (Xiao et al., 2022; Zhang et al., 2023a).

Prior works on Few-shot Learning (FSL) (Wang et al., 2024), transfer learning (Dhekane & Ploetz, 2024), and cross-domain FSL (Thukral et al., 2025; Yin et al., 2024) reduce data collection costs by adapting pre-trained models to sensing applications. However, they typically rely on large-scale labeled datasets within the same modality to costly train source models from scratch (Song et al., 2023), or face challenges such as *modality shift* with limited transferability when leveraging pre-trained models (Oh et al., 2022; Tao et al., 2022; Guo et al., 2022), particularly in cross-modality settings. Recent advances in multi-modal learning (Yang et al., 2023; Chen & Yang, 2025; mengxi Chen et al., 2024; Madaan et al., 2024; Yang et al., 2024; Baldenweg et al., 2024) (e.g., CLIP-based models (Girdhar et al., 2023; Wu et al., 2023; Moon et al., 2023)) and cross-modal learning

(e.g., image-to-sensor distillation (Zhao et al., 2018; Song et al., 2022; Gurbuz et al., 2020; Zhang et al., 2023c) or alignment-based transfer (Kamboj et al., 2025; Chen et al., 2024)), further demonstrate the feasibility of knowledge transfer across modalities. However, they remain modality-specific (i.e., relying on shared semantic feature spaces), and typically require large-scale unlabeled and paired data with resource-intensive training and deployment, leading to high costs and making them impractical for few-shot adaptation to support human sensing at the edge. These gaps motivate a *scalable* and *adaptable* model transfer that can broadly reuse pre-trained models across modalities (e.g., vision or text) for new sensing modalities (e.g., radar or bio-signals) using only few data.

In practice, however, addressing this need is uniquely challenging. Due to substantial differences in data characteristics, such as shape, distribution, and feature representation, between source and target modalities (i.e., *modality shift*), transferred models often suffer from significantly degraded performance (i.e., *negative transfer*) (Guo et al., 2022; Oh et al., 2022). Our experiments reveal that state-of-the-art (SOTA) baselines (Table 1) fail to reach oracle performance (Gong et al., 2019) and suffer from substantial *overfitting* when applied to human sensing tasks with few data, falling notably short of the *goal*, as shown in Figure 1(a). These highlight the underlying challenge of *latent feature distribution misalignment* across modalities. Also, these methods often neglect *resource constraints*, rendering them impractical for edge deployment, especially in advanced multi-source settings (Zhao et al., 2020; Yue et al., 2021a; Lee et al., 2019). While model structuring methods such as neural architecture search (NAS) (Wen et al., 2023; Han et al., 2021), pruning (Frankle & Carbin, 2019; Shen et al., 2022), or quantization (Polino et al., 2018), aim to reduce resource demands, they often fail to maintain performance under modality shift and few data. As shown in Figure 1(c), our experiments using pruning (Shen et al., 2022) demonstrate significant model accuracy loss by 50.5% on average.

Driven by the increasing availability of high-quality pre-trained models from public repositories (e.g., PyTorch Hub (Hub, 2022)), we propose XTransfer, a first-of-its-kind method enabling modality-agnostic, few-shot model transfer. It flexibly leverages public pre-trained models and transfers knowledge across modalities (e.g., image, text, audio, or sensing) to human sensing tasks using only few labeled sensor data with no additional unlabeled data (i.e., *cross-modality FSL settings*, Appendix A.1), significantly reducing the costs of large-scale data collection and training from scratch. Its resource-efficient design also optimizes both cloud performance and edge deployment, enabling scalable and adaptable method across human sensing applications.

Instead of relying on shared semantic spaces or paired cross-

modal data, XTransfer mitigates modality shift by *model repairing* at the level of *layer-wise* latent feature distribution misalignment using activation-based statistics. This layer-wise formulation is motivated by our observation (Section 3) that modality shift “damages” intermediate representations unevenly across layers, making global adaptation with few data unstable and prone to overfitting. It is enabled by a Splice–Repair–Removal (SRR) pipeline (Section 4) that (i) splices heterogeneous layer inputs, (ii) repairs layer misalignment via an anchor-based generative transfer module in a reduced-orthogonal feature space, and (iii) removes unnecessary channels after repair. Building on the insight that not all repaired layers contribute, XTransfer further features *layer recombining* using a Layer-Wise Search (LWS) control (Section 5) that selects and recombines *layers of interest* (i.e., useful repaired layers) through an NAS-inspired, resource-constrained layer-wise search, incrementally enhancing the repairing and optimizing model structure. To *accelerate* and *stabilize* LWS in multi-source settings with large candidate pools, we incorporate a *pre-search check* strategy coupled with a *dynamic search range* mechanism to avoid unnecessary repairing, balancing accuracy and efficiency. The main contributions are summarized as:

- A first-of-its-kind method, XTransfer, that enables modality-agnostic, few-shot model transfer with resource-efficient design for human sensing on edge systems.
- A SRR pipeline that mitigates modality shift and prevents overfitting via layer-wise repairing of latent feature distribution misalignment.
- A LWS control that enables efficient, stable layer-wise search, selectively recombining layers of interest while discarding others for model restructuring.
- Extensive experimental evaluations (Section 6) under cross-modality FSL settings, benchmarking SOTA baselines (Table 1) on various source and target datasets (Table 2), showing consistent accuracy and efficiency gains.

## 2. Related Work

**Learning with few data for human sensing.** Recent works in FSL and cross-domain FSL have proposed *single-* and *multi-source* methods. Single-source methods align latent features between source models and target data via distance-based objectives (Zhao et al., 2021; Yue et al., 2021b), whereas multi-source methods leverage the Wisdom of the Crowd principle through unsupervised source distillation (Zhao et al., 2020; Yue et al., 2021a) or maximal correlation analysis (Lee et al., 2019). Recent efforts have also

<sup>1</sup>We test a pre-trained ResNet18 on miniImageNet as source and HHAR dataset as target under a 5-shot setting with LOOCV enabled (details in Appendix A.2).

<sup>2</sup>The number of classes in the source model should be greater than that in the target.

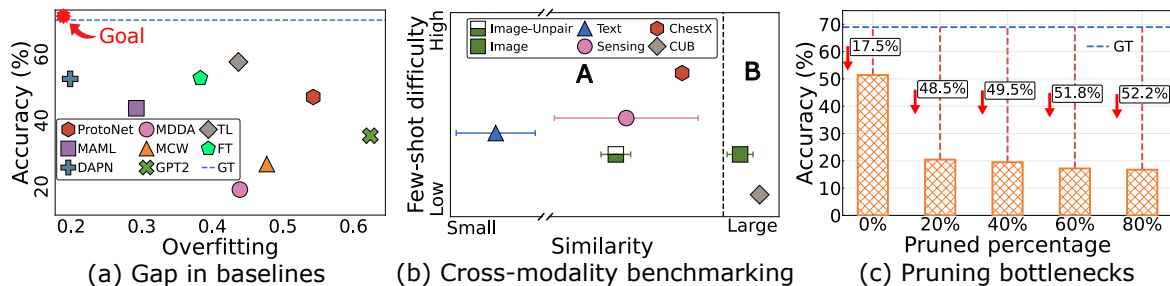


Figure 1. Preliminary study under cross-modality FSL settings<sup>1</sup>. (a) reveals baseline performance gap. (b) shows average similarity and FSL difficulty across all target sensing datasets in Table 2 to source modalities (*e.g.*, Image, Text, Sensing) using default reshaping (Appendix B.1) and benchmarking (Oh et al., 2022) (Appendix A.2 for details). Two distinct areas represent similarity levels (A–hard, B–normal). Key findings: 1) compared to CUB, similarity levels across modalities are notably low, *e.g.*, Text and Sensing fall into Area A, indicating a significant modality shift; 2) compared to Image-Unpair (*i.e.*, no class pairing) in Area A, Image surprisingly falls into Area B, indicating that pairing classes<sup>2</sup> may enhance cross-modality similarity; 3) Image exhibits more stable standard deviations and lower FSL difficulty, suggesting better potential for model transfer. (c) shows significant model accuracy loss using pruning.

explored fine-tuning LLMs (*e.g.*, GPT2 (Zhou et al., 2023)) for time-series analysis. However, testing on benchmarks (Liang et al., 2021; Oh et al., 2022), our results reveal that they suffer from severe overfitting under cross-modality FSL settings. LLM-based data augmentation (Leng et al., 2024; 2023) helps reduce data collection costs, but remains modality-specific and orthogonal to our focus. Recent advances introduce foundation models (FM) (Abbaspourazad et al., 2024; Weng et al., 2024) or prompt-based FM adaptation (Li et al., 2025) for human sensing, but these methods assume either a pre-existing target-modality FM or access to large-scale unlabeled and paired data for feature alignment. Existing attempts in human sensing FSL (Gong et al., 2019; Wang et al., 2024; Thukral et al., 2025; Yin et al., 2024) remain constrained by a strong reliance on learning in the same modality, resulting in costly source data collection and training. In contrast, XTransfer enables layer-wise model repairing to safely mitigate modality shifts using only few sensor data, achieving significant cost reduction.

**Model structuring for edge deployment.** Model structuring techniques such as pruning (Frankle & Carbin, 2019; Shen et al., 2022), quantization using low-precision data types (Polino et al., 2018), model merging by fine-tuning shared layers (Padmanabhan et al., 2023), one-size-fits-all model (Cai et al., 2020), and NAS techniques such as model restructuring (Wen et al., 2023; Han et al., 2021) or search using few data (Eustratiadis et al., 2024; Xu et al., 2022), have shown success in reducing model resource overhead. However, they strongly rely on either sufficient target datasets or minimal modality shifts to maintain model performance. XTransfer uniquely applies layer recombining to optimize model structures while strengthening repaired layer-wise dependence at scale under cross-modality FSL settings. It not only restructures models for streamlined edge deployment but also enhances model repairing.

### 3. Preliminary

**Layer-wise analysis.** It is widely used to diagnose representation quality and guide model restructuring (Sahoo et al., 2025). We examine how accuracy and latent feature discriminability change across layers. Since effective training relies on discriminative latent representations (Islam et al., 2021), we quantify layer-wise latent features using Mean Magnitude of Channels (MMC) (Luo et al., 2022) as a lightweight activation-based statistics. We also measure class clustering via the Silhouette score (S-score) (Shahapure & Nicholas, 2020) computed on MMC-based representations, which captures inter-/intra-class distances and reflects layer-wise discriminability. We segment the backbone into  $L$ -units, defined as a single layer or an inseparable dependent layer block (L-Blocks in Table 3) that cannot be structurally decoupled (*e.g.*, residual blocks in ResNet). The experimental setup is detailed in Appendix A.3, and additional evidence on S-score/accuracy correlation is provided in Appendix A.4. Figure 2(a) shows that negative transfer (Zhang et al., 2023b) disrupts accuracy convergence across layers (*i.e.*, impaired layer-wise dependence), leading to misalignment and accuracy drops under few-shot fine-tuning. These degradations correlate with MMC shifts, where larger shifts correspond to larger accuracy drops (Figure 2(b)). We adopt MMC as a modality-agnostic metric as it is defined purely on layer activations without assuming shared semantic spaces or paired data, remaining lightweight and stable under FSL settings, compared to kernel-based distribution metrics such as Maximum Mean Discrepancy (MMD) (Wang et al., 2023).

**Problem setup.** We aim to minimize *layer-wise MMC shifts* under cross-modality FSL settings. This poses several challenges that motivate the design of SRR pipeline and LWS control: (i) cross-modality transfer must handle structural differences (*e.g.*, input formats and feature shapes) and semantic discrepancies (*e.g.*, non-overlapping label spaces), requiring an objective defined purely on latent represen-

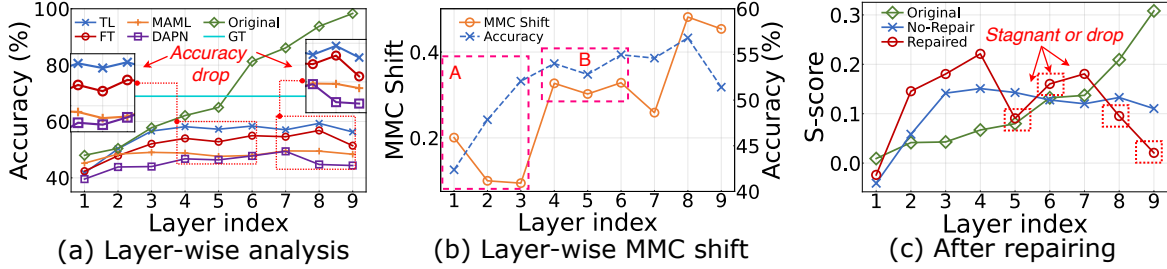


Figure 2. Design insights. (a) Layer-wise accuracy convergence using baselines is disrupted due to modality shift. (b) In area A, accuracy rises as MMC shift stays low, indicating a small latent feature gap. In area B, MMC shift notably increases with layer index, where excessive latent feature deviation begins to reduce accuracy. (c) After repairing, S-score improves but stagnation occurs at certain layers.

tations (e.g., activation-based MMC statistics) rather than shared semantic spaces or paired data; (ii) the latent feature distribution misalignment is complicated by *noisy* representations and strong layer-wise dependencies inherited from pre-training, making few-shot repair brittle; and (iii) not all layers remain useful after repairing (Figure 2(c)), selectively recombining useful layers is critical and must be done efficiently and stably in multi-source settings with large candidate pools. Figure 3 overviews XTransfer.

## 4. Model Repairing

Enabled by SRR pipeline, this process safely repairs layer-wise misalignment by minimizing MMC shifts, restoring pre-trained layer performance under cross-modality FSL settings. As shown in Figure 3, SRR comprises three stages. **Splice:** instead of default reshaping using fixed up/down-sampling (Appendix B.1), which is non-trainable and can discard features, especially when layer shapes vary during layer-wise search, we propose a trainable, compact *connector* placed between heterogeneous layers to enforce shape compatibility, consisting of a Pre-header (adaptive convolutional layer), Resizer, and one encoder-decoder pair. **Repair:** each connector is fine-tuned by the *generative transfer module* to adapt layer channels and minimize MMC shifts. **Removal:** *layer channel removal* (Appendix B.2) is applied to further strengthen repairing.

### 4.1. Repairing in complex feature space

Since source layers are already highly discriminative, our intuition is to *safely* adapt few sensor data by aligning their misaligned latent feature distributions to the "original" source-layer distributions, which serve as *anchors*. We hence propose cross-modality *anchor-based* alignment, which aligns source MMCs as *anchors* (i.e., anchor MMCs) with sensing MMCs. Since the raw MMC feature space is high-dimensional, noisy and correlated across channels, our insight is to reduce MMC dimensionality by preserving key layer channels while suppressing noise.

**Reduced-orthogonal feature space.** For each layer, we project anchor MMCs into a low-dimensional, orthogonal

feature space via PCA (Valpola, 2015) (i.e., *anchor PCA space*). PCA removes redundancy by decorrelating channel dimensions and suppresses noise, yielding a compact subspace (we use 2 components by default) that preserves maximal variance and typically forms highly clustered class distributions. The resulting projection coefficients (i.e., *component weights*) also highlight the most important layer channels that contribute to layer performance. Given high discriminability of the original layers, the projected anchor MMCs preserve high clustering performance, with class distributions tightly centered (i.e., *Anchor-center*), as shown in Figure 3(a). Once initialized per layer, the same anchor PCA space is reused to project sensing MMCs.

**Feature space alignment.** After projection, we observe that the sample distribution for each class, along with their centroid (i.e., *Sensing-center*), appears disorganized compared to the well-clustered *Anchor-center* at each layer, as shown in Figure 3(a). Due to MMC shifts, the *scale* and *orientation* of *Sensing-center* are notably different from those of *Anchor-center*. To align the scale, we first define a scale function based on the mean shift in inter-class distance  $\text{InterD}(\cdot)$ , formulated as  $S = \text{Mean}(\text{InterD}(\text{Pro}(f_{s_{ij}}))) / \text{Mean}(\text{InterD}(\text{Pro}(f_{t_{ij}})))$ , where  $\text{Pro}(\cdot) = \text{PCA}(\text{MMC}(\cdot))$  denotes the space project function,  $f_s$  and  $f_t$  represent the latent features from both source and sensing modalities, respectively.  $i$  denotes the index of pre-trained models, and  $j$  denotes the layer index in each model  $i$ . Next, to align the orientation, we design a rotation alignment function that minimizes the cosine angle (Nguyen & Bai, 2010) by fine-tuning a multi-dimensional rotation matrix  $[M_{rot}]$  with dimensions matching the number of PCA components:

$$\arg \min_{[M_{rot}]} \text{Cos}(\text{Cen}(\text{Pro}(f_{s_{ij}})), \text{Cen}(\text{Pro}(f_{t_{ij}}) * S) \cdot [M_{rot}]) \quad (1)$$

where  $\text{Cos}(\cdot)$  denotes the cosine similarity function, and  $\text{Cen}(\cdot)$  calculates the centroid of the projected distribution. Figure 3(b) shows the aligned results.

**Anchor class pairing.** Building on the key finding that class pairing boosts latent feature alignment across modalities in Figure 1(b), we propose selecting source classes with

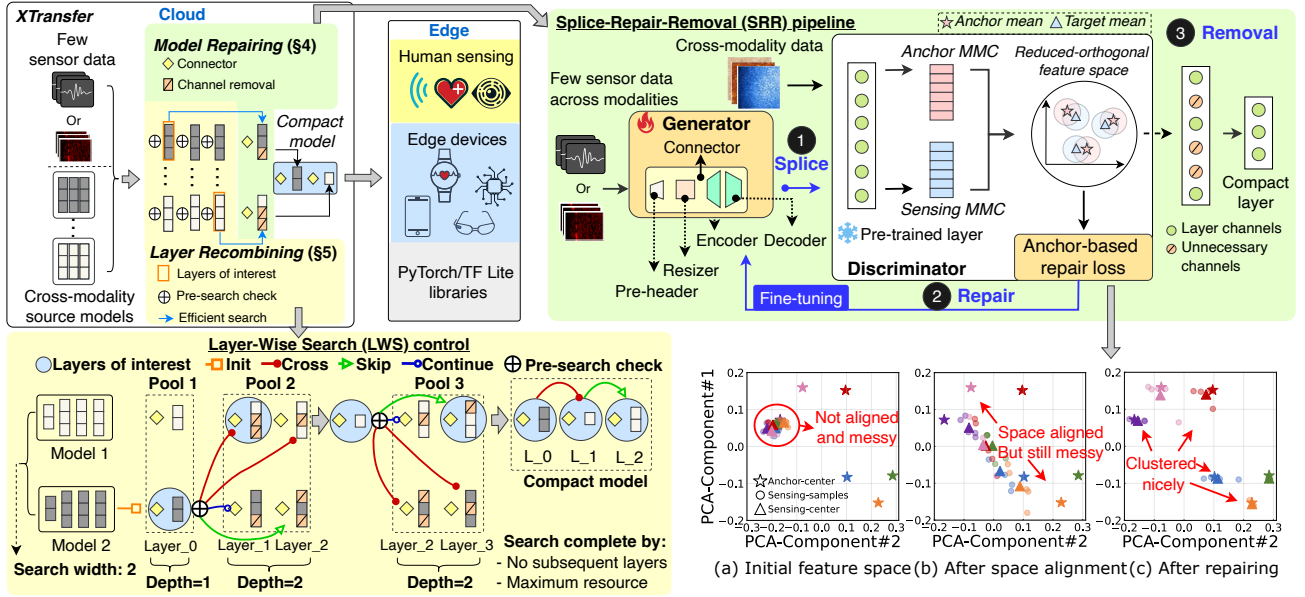


Figure 3. Overview. XTransfer transfers source models across modalities with few sensor data through model repairing (SRR pipeline) and layer recombining (LWS control). LWS control first segments source models into layers and operates layer-wise search across pools. At each pool, the pre-search check decides which layers need repairing, then SRR pipeline repairs them and LWS control selects layers of interest. These layers are incrementally recombined during the search, restructuring models for enabling human sensing at the edge. Subfigures (a)–(c) illustrate the feature space evolution before and after repairing.

the highest S-scores as *anchor* classes to pair with sensing classes by minimizing a pairing shift objective (*i.e.*, sum of centroid distances across pairs). This is solved as a linear sum assignment via the standard Hungarian algorithm, outputting the optimal pairing set  $pairST$ . This pairing is fully optimized by similarity in the given feature space.

## 4.2. Repairing layer-wise dependence

**Generative transfer module.** To restore layer-wise dependence, we design a *generative transfer module* that optimizes the generator (*i.e.*, connector) using an adversarial objective. The discriminator operates on each frozen pre-trained layer together with its anchor PCA space (Figure 3). Freezing preserves stable anchors and prevents overfitting. Given each pairing set  $pairST$ , the connector is fine-tuned to minimize MMC shifts, uniquely transforming sensor inputs to align with anchors.

**Anchor-based repair loss.** We propose an *anchor-based repair loss* ( $loss_{srr}$ ) to harmonize layer-wise latent feature distributions across modalities in the anchor PCA space. For each class pair  $(c_s, c_t) \in pairST$ , our objective (i) *minimizes* the distance  $D(\cdot)$  between the centroids of the projected anchor and sensing MMC distributions (*i.e.*, positive loss), and (ii) *maximizes* the distance between sensing MMC samples with different labels ( $c_t^-$ ) (*i.e.*, negative loss). Since the projected anchor MMCs are highly clustered, they can provide the maximum *margin* ( $M_{max}$ ) between anchor clusters. To further improve the negative loss, we

update the function by calculating the *anchor-based margin*  $margin^c = InterD(Pro(fs_{ij}^{c_s})) - IntraD(Pro(fs_{ij}^{c_t}))$ , where the  $M_{max}$  is selected, and  $IntraD(\cdot)$  measures the intra-class distance. The loss function is formulated as:

$$loss_{srr} = \frac{1}{N} \sum_{(c_s, c_t) \in pairST} D(Cen(Pro(fs_{ij}^{c_s})), Cen(Pro(ft_{ij}^{c_t}))) + \frac{1}{K} \sum_{(c_t, c_{tk}^-)} ReLU(M_{max} - D(Pro(ft_{ij}^{c_t}), Pro(ft_{ij}^{c_{tk}^-}))) \quad (2)$$

where  $K$  denotes the number of negative samples, and  $N$  denotes the number of classes. The  $ReLU(\cdot)$  is used to trigger the negative loss in the condition where the distance between the samples is less than  $M_{max}$ . Figure 3(c) shows the effectiveness of model repairing.

## 5. Layer Recombining

Working with the SRR pipeline, XTransfer performs *layer recombining* via LWS control to (i) perform the pre-search check that accelerates the search, (ii) stabilize the search using the dynamic search range mechanism, and (iii) select and recombine layers of interest to restructure models.

### 5.1. Search control design

Inspired by NAS (White et al., 2023), effective layer-wise search relies on properly designing the search space, actions, and strategy under on-device resource constraints. We hence define the search space as all layers from source models,

organized into *search pools* containing layer candidates (i.e., repaired layers). Each pool forms a window of size  $I \times J$ , where  $I$  is the number of source models (width) and  $J$  is the number of L-units (depth). We also define four search actions: *init* selects a starting layer (default depth 1); *continue* and *skip* perform intra-model recombination; and *cross* enables inter-model recombination.

**Resource-constrained search strategy.** To effectively control search actions within each search pool, we propose a layer value function based on the S-score  $Score(\cdot)$  to evaluate each repaired layer performance and the convergence between adjacent layers after each SRR process  $SRR(\cdot)$ . It is formulated as  $V_{ij} = Score(SRR(Pro(ft_{ij}), MT_{ij}, L_{ij}), Y_t)$ , where  $MT_{ij}$  is the connector and  $L_{ij}$  is each repaired layer. Under resource constraints, LWS control selects the highest-valued candidate in each pool and verifies that it improves layer-wise dependence by checking whether its S-score exceeds that of the previously selected layer. If selected,  $L_{ij}$  becomes a *layer of interest* and is recombined, and the next pool starts from layer index  $j + 1$ . Otherwise, the pool is discarded, and the window shifts forward. To incorporate the constraints, we define a resource-constrained function formulated as  $RC(n) = exp(n/(L-2)-2)+1, n \in [1, L]$  where  $n$  is the current recombined layer index and  $L$  is the maximum number of L-units. Each candidate’s adjusted overhead is computed as  $R(n)_{ij} = (Res(L_{ij}) * RC(n))/Max(Res(P))$ , where  $Res(\cdot)$  measures actual cost (e.g., weighted FLOPs and memory), and  $Max(Res(P))$  is the maximum cost in current pool  $P$ . The resource-constrained layer value function becomes  $VR_{ij} = V_{ij} / R(n)_{ij}$ . The objective is defined as  $\arg \max_{L_{ij} \in P} VR_{ij}, s.t. \sum_0^n Res(L_{ij}) \leq R_{Max}$ , where  $R_{Max}$  is device-specific resource budget.

## 5.2. Efficient search

**Pre-search check.** Although SRR fine-tunes connectors efficiently, applying SRR to every candidate in a large pool can still slow down LWS control. We hence propose the *pre-search check* strategy that avoids unnecessary repairs *before* applying SRR. We track S-score progression across three states: after anchor pairing (Anchor) (i.e., repairing objective), before SRR (Before), and after SRR (After). Empirically, SRR improves S-scores from Before to After, approaching the Anchor level, indicating a strong correlation (see Appendix B.3 for details). Based on this insight, our intuition is to estimate repaired S-score (i.e., repair rate) of each layer based on Before and Anchor states to decide whether to bypass unnecessary repairs. Experiments show the actual repair rate grows exponentially with the recombined layer index (Appendix B.4). We hence design a *repair rate growth model* formulated as  $rate_n^{est} = exp(a * n) + b, n \in [1, L]$ , where  $a$  and  $b$  are optimized via non-linear regression to min-

imize MSE to fit  $rate_n^{est}$ , with the objective defined as  $\arg \min_{a,b} \frac{1}{n'} \sum_{n=0}^{n'} (rate_n^{est} - rate_n)^2$ , where  $n'$  is the number of recombined layers. Estimation starts after *init* and is updated after each newly selected layer.

**Dynamic search range mechanism.** Using  $rate_n^{est}$ , LWS can initially apply a narrow search range (e.g., only the top-1 candidate by estimated repair rate) to filter most candidates *before* SRR. However, since  $rate_n^{est}$  is updated sparsely, estimation errors may cause missed optimal candidates. To stabilize search while retaining efficiency, we develop a dynamic search range mechanism that adjusts the search range, which is formulated as  $range_n = (1 + \hat{u} \pm rate_n^{est}) * range_{n-1}$ ,  $range_n \in [0.2, 1]$ , where the range starts at 0.5 and adjusts based on the previous range. Here,  $\hat{u}$  is a signed unit vector. If  $rate_{n-1}^{est} < rate_{n-1}$ , it indicates that the estimation might be inaccurate, and  $\hat{u}$  will be positive to increase the search range to repair more candidates and stabilize accuracy. Otherwise, the range will be decreased to bypass unnecessary repairs and improve efficiency.

## 6. Experiment

### 6.1. Experiment setup

We benchmark XTransfer against SOTA baselines, grouped into single- and multi-source methods (Table 1). Evaluation is conducted on 8 widely-used public datasets under cross-modality FSL settings (Table 2), using their corresponding public pre-trained models as sources, from diverse modalities (e.g., image, text, audio, and sensing) with various backbones such as ResNet18 from PyTorch Hub (Hub, 2022) (Table 3). To evaluate XTransfer, we develop 4 real-world applications and build testbeds on 3 commercial edge devices (e.g., smartwatch, smartphone, Raspberry Pi, Appendix Table 5 for details).

Based on the testbeds, we collect 4 human sensing datasets (marked as Private in Table 2) as targets, from 40 participants in real-world settings, with ethics approval from the Human Research Ethics Committee of our institute. Additionally, we include 2 public sensing datasets and 1 image dataset as targets for standard benchmarking. We apply standard Leave-One-Out Cross-Validation (LOOCV) (Gong et al., 2019) for evaluating human sensing datasets, and adopt accuracy-to-resource (ATR) ratio, defined as  $ATR = Accuracy / (\alpha Norm(FLOPs)) + (1 - \alpha) Norm(Params)$  for evaluating resource-accuracy efficiency, where  $\alpha$  is set to 0.5 by default (Appendix A for more details on our experiment setup).

### 6.2. XTransfer performance

**Repair performance.** We first evaluate how our Repair loss reduces MMC shift to enhance each layer’s S-score with

Table 1. State-of-the-art (SOTA) baselines.

Baselines	Group	Description
Transfer Learning (TL) (Jiang et al., 2022)	Single-source	A standard transfer learning method that reuses a source model by <b>freezing all layers</b> .
Fine-tuning (FT) (Oh et al., 2022)	Single-source	A conventional fine-tuning method that <b>updates all layers</b> of a pre-trained model using available target data.
ProtoNet (Chen et al., 2019)	Single-source	A distance-based FSL method that constructs <b>class prototypes</b> by averaging support set and classifies query set in the feature space.
MAML (Chen et al., 2019)	Single-source	A gradient-based meta-learning method that learns a source model with <b>shared initialization parameters</b> from scratch.
DAPN (Zhao et al., 2021)	Single-source	A cross-domain FSL method that uses <b>adversarial ProtoNet</b> with a domain discriminator to reduce latent feature distribution shift.
SemiCMT (Chen et al., 2024)	Single-source	A cross-modal learning method that applies <b>contrastive self-supervised learning</b> during model adaptation.
GPT2 (Zhou et al., 2023)	Single-(LLM)	A LLM-based method that enables <b>in-context learning</b> after fine-tuning on few target data.
MDDA (Zhao et al., 2020)	Multi-source	A multi-domain FSL method that uses <b>adversarial discriminative adaptation</b> and <b>multi-source knowledge distillation</b> .
MCW (Lee et al., 2019)	Multi-source	A multi-domain FSL method that uses <b>maximal correlation analysis</b> to fuse multiple source domains for few-shot model adaptation.
MetaSense (Gong et al., 2019)	Oracle-(GT)	An advanced FSL method based on MAML that uses <b>extensive target data</b> to train from scratch, serving as an oracle upper bound.

Table 2. Source and target datasets specifications.

Dataset	Modality	Subject	Class	Train Size	Type	Shape	Privacy
<b>Source</b>							
miniImageNet (Vinyals et al., 2016)	Image	-	100	50k	-	3x84x84	Public
miniDomainNet (Zhou et al., 2021)	Image	-	126	137.5k	-	3x224x224	Public
Office-31 (Saenko et al., 2010)	Image	-	31	3.3k	-	3x224x224	Public
Office-Home (Venkateswara et al., 2017)	Image	-	65	12.7k	-	3x224x224	Public
Caltech-101 (Fei-Fei et al., 2004)	Image	-	101	7.3k	-	3x224x224	Public
Newsgroup (Thulasidasan et al., 2021)	Text	-	20	15k	-	1000x1x1000	Public
VoxCeleb (Nagrani et al., 2017)	Audio	-	100	14.9k	Time-S	1x512x300	Public
OPPORTUNITY (Roggen et al., 2010)	IMU	12	11	3.7k	Time-S	77x1x100	Public
<b>Target</b>							
HHAR (Sisen et al., 2015)	IMU	9	6	-	Time-S	6x1x256	Public
WESAD (Schmidt et al., 2018)	ECG	15	3	-	Time-S	10x1x256	Public
Gesture	IMU/PPG	10	8	-	Time-S	7x1x200	Private
Writing	Ultrasound	10	10	-	Time-S	1x1x256	Private
Emotion	mmWave	10	7	-	Spectrum	3x224x224	Private
BP	mmWave	10	-	-	Doppler	1x1x499	Private
ChestX (Wang et al., 2017)	Image	-	5	-	-	1x1024x1024	Public

Table 3. DL model backbone specifications.

Backbone	Layers	L-Blocks	GFLOPs	Params	Kernel	Shape
ResNet18 (Chen et al., 2019)	18	9	3.67	11.18M	2D	3x224x224
ResNet18-1D (Chen et al., 2019)	18	9	0.39	3.9M	1D	100x1x1000
Multi-Conv4 (Zhao et al., 2020)	4x5	4	0.3	1.15M	2D	3x32x32
Multi-ResNet10 (Zhao et al., 2020)	10x5	5	0.7	24.5M	2D	3x84x84
Multi-ResNet18 (Zhao et al., 2020)	18x5	9	18.35	55.9M	2D	3x224x224
Conv4 (Chen et al., 2019)	4	4	0.02	0.07	1D	1x1x500
Conv5 (Gong et al., 2019)	5	5	0.19	30.42M	1D	By Input
GPT2 (Zhou et al., 2023)	4x6	6	0.41	82.9M	1D	By Input

different MMC dimensionalities. We use HHAR and the standard pre-trained ResNet18 on miniImageNet under 5-shot setting. The layer channel removal is disabled. We test with 4 different levels of MMC dimensionality (*i.e.*, number of layer channels) ranging from 64 to 512. We employ N-Pair loss (Zhang et al., 2023c) and Triplet loss (Weller et al., 2022) in FSL sensing tasks as baselines. We run 15 rounds for each setting by default throughout the evaluation. Figure 4(a) presents that our Repair loss consistently achieves the highest S-score of 0.2 on average, outperforming both N-Pair loss (0.05) and Triplet loss (0.07), across all levels of MMC dimensionality. It indicates that Repair loss effectively enhances layer performance.

**Efficient search performance.** We now evaluate LWS control performance regarding model accuracy and layer search efficiency. We employ HHAR as target, ResNet18 on miniImageNet and Multi-ResNet18 on 5 image datasets as sources shown in Table 2, with a default *search depth* of 3 in 3-, 5- and 10-shot settings. We also utilize MetaSense in Table 1 as the oracle baseline. We compare different configurations: ResNet18 (Single) and Multi-ResNet18 (Multi) without efficient search enabled, Multi-ResNet18 (Multi-Pre) with only pre-search check using top-1 layer selection

enabled, and Multi-ResNet18 (Multi-Efficient) with both pre-search check and dynamic search range enabled. As shown in Figure 4(b), Multi-Pre achieves a lowest search time on average across all n-shot settings, but it leads to degraded accuracy by 3.36% and 7.94% on average, respectively, compared to Multi and Multi-Efficient. It also fails to reach oracle-level accuracy and presents the highest standard deviation on average. The results indicate that relying solely on the pre-search check introduces search stability issues due to inaccurate or drifted repair value estimation. In contrast, Multi-Efficient provides a strong balance between accuracy and efficiency. It reduces search time by 2.1 to 4 times compared to Multi in 5- and 10-shot settings, while outperforming the oracle baseline. While Multi-Efficient takes a longer search time than both Single and Multi-Pre, it successfully achieves superior accuracy and search stability, highlighting the benefits of using multiple source models and dynamic search range mechanism. Notably, even the search space is expanded 5 times more compared to Single, Multi-Efficient requires only 2.1 times more search time, indicating strong scalability enabled by the efficient search. The results also reveal that both Multi-Efficient and Multi achieve lower standard deviation on average compared to Single, suggesting that using multiple source models offers commendable search stability. In short, the results prove that the proposed efficient search significantly accelerates the layer search process while improving accuracy and stability.

**Impact of different sources.** Since the selection of pre-trained source models plays a crucial role in XTransfer, we evaluate how different source models from various modalities affect the accuracy and resource overhead of the output models. We use HHAR, 2 pre-trained ResNet18s on both miniImageNet (Image) and VoxCeleb (Audio), and 2 pre-trained ResNet18-1Ds on both Newsgroup (Text) and OPPORTUNITY (Sensing), as shown in Table 2. We keep the other experimental setups unchanged and include 2-shot settings. Figure 4(c) shows that the output models using Image source achieve the highest accuracy of 70.5% on average in 3- to 10-shot settings, compared to that of 69.6%, 64.3%, and 67% achieved by using Text, Audio, Sensing sources, respectively. This suggests that the latent features learned from Image, trained on larger datasets with broader class semantics, provide higher discriminability than those

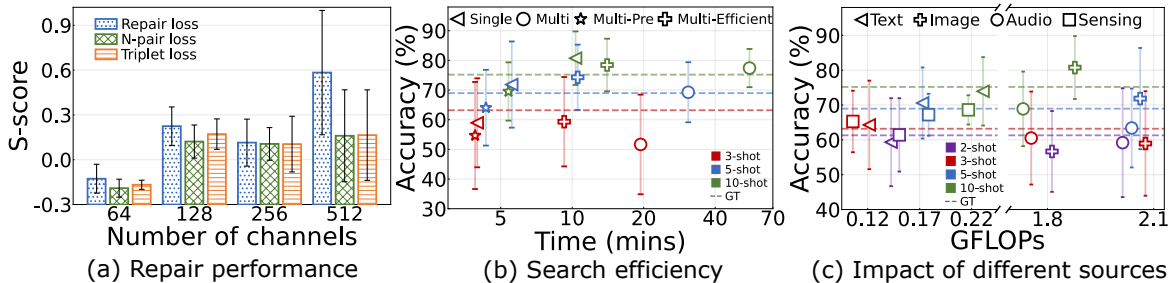


Figure 4. Ablation study evaluating the performance of model repairing and layer recombining.

Method	HHAR (%)			WESAD (%)			Gesture (%)			Writing (%)			Emotion (%)			ChestX (%)		
	3-shot	5-shot	10-shot															
MetaSense (Gong et al., 2019)	63.2	69.0	75.2	55.1	64.0	68.3	66.3	73.4	79.4	72.1	83.3	89.6	55.5	56.3	65.5	24.8	28.1	31.7
ProtoNet (Chen et al., 2019)	50.6	45.7	49.8	43.9	49.3	52.0	<b>50.8</b>	55.8	59.2	69.5	78.7	73.4	<b>51.3</b>	49.2	54.8	21.7	23.4	24.5
DAPN (Zhao et al., 2021)	48.7	51.2	54.7	56.9	61.2	63.1	45.8	49.4	50.5	<b>75.1</b>	78.6	79.6	48.0	50.0	<b>58.7</b>	24.0	24.4	25.5
MAML (Chen et al., 2019)	36.6	42.3	42.4	39.6	57.9	65.6	37.2	41.3	39.4	31.6	39.7	35.2	22.3	26.9	31.1	22.5	20.4	21.9
SemiCMT (Chen et al., 2024)	33.3	38.9	48.9	37.3	40.0	44.4	23.5	34.4	42.5	27.3	38.6	48.0	24.0	33.6	46.7	25.3	25.6	28.0
GPT2 (Zhou et al., 2023)	41.0	34.0	45.0	48.0	35.0	36.0	<b>49.0</b>	54.0	63.0	52.0	71.0	75.0	-	-	-	-	-	-
Our-Single	<b>59.0</b>	<b>71.8</b>	<b>80.7</b>	<b>77.9</b>	<b>78.4</b>	<b>81.8</b>	45.2	<b>69.6</b>	<b>77.8</b>	72.8	<b>87.0</b>	<b>91.3</b>	<b>43.6</b>	<b>55.6</b>	<b>61.4</b>	<b>27.7</b>	<b>28.6</b>	<b>30.4</b>
MDDA (Zhao et al., 2020)	13.2	17.7	18.8	40.0	39.3	41.9	11.2	13.9	15.2	12.5	10.9	9.0	14.4	15.3	16.0	20.6	19.6	19.9
MCW (Lee et al., 2019)	27.6	25.4	26.9	30.7	32.7	32.4	22.3	23.4	25.6	32.3	31.6	30.2	25.3	27.2	26.5	22.4	21.5	22.8
Our-Multi	<b>59.3</b>	<b>74.3</b>	<b>78.4</b>	<b>76.4</b>	<b>77.8</b>	<b>78.7</b>	48.7	<b>73.1</b>	<b>78.6</b>	<b>74.1</b>	<b>86.1</b>	<b>90.4</b>	42.3	<b>55.1</b>	58.6	<b>29.0</b>	<b>30.0</b>	<b>30.2</b>

Table 4. Comparison in model accuracy. Top-2 results are highlighted in bold.

learned from other modalities. Notably, Image achieves lower average accuracy in 2- and 3-shot settings, suggesting that extremely low target data may not fully represent the test data distribution, leading to less stable alignment when using Image source. In contrast, both Text and Sensing result in higher average accuracy and reach the oracle, indicating that performance varies with source model quality and semantic relevance to the target. These results also show that XTransfer can flexibly reuse diverse source models across modalities to improve ultra low-shot performance. Moreover, the output models using Text or Sensing sources require only 0.16G FLOPs on average, as 1D kernels require much less computation than 2D kernels. Since XTransfer prioritizes accuracy, we select Image source models by default. More ablation results see Appendix C.

### 6.3. Comprehensive comparison

**Cross-modality FSL performance.** We evaluate the overall performance of XTransfer regarding both accuracy and ATR across 5 sensing datasets and 1 image dataset as targets (Table 2). We compare XTransfer against a range of SOTA baselines shown in Table 1. We report two variants with different sources: *Our-Single*, using a ResNet18 pre-trained on miniImageNet, and *Our-Multi*, using Multi-ResNet18 with five corresponding image datasets. We additionally report GPT2-small fine-tuning for comparison, following the parameter setting in (Zhou et al., 2023). All methods on target datasets are evaluated under the same cross-modality FSL settings (Appendix A.1), where only few target data are fine-tuned with sources. MetaSense

(Gong et al., 2019) serves as the oracle, trained on Conv5 with sufficient target sensor data (Table 3). For consistency, we also train the oracle using ResNet18 on the Emotion dataset to match 2D kernels. As shown in Table 4 and Appendix Table 12, both our variants outperform the baselines regarding model accuracy and ATR, and successfully reach or surpass the oracle in model accuracy across all target datasets in 5- and 10-shot settings. Specifically, both *Our-Single* and *Our-Multi* achieve a significantly higher ATR on average, surpassing the existing single- and multi-source baselines by 1.6 to 29 times and 16.6 to 98 times, respectively. While our variants are slightly below the oracle on HHAR, Gesture, and Emotion under 3-shot settings, XTransfer can further improve by reusing source models with higher quality or closer semantic relevance, as shown in our source-impact study. Overall, XTransfer achieves SOTA accuracy while substantially reducing data and resource costs, providing a scalable and adaptable method for human sensing at the edge. More results see Appendix C.

## 7. Conclusion

This paper presents XTransfer, a novel method that enables modality-agnostic few-shot model transfer with resource-efficient design. XTransfer reuses the power of pre-trained models as free sources and requires only few sensor data to restructure models. It significantly reduces the costs associated with sensor data collection, model training, and edge deployment, offering a scalable and adaptable method for advancing human sensing applications.

## References

- Abbaspourazad, S., Elachqar, O., Miller, A., Emrani, S., Nallasamy, U., and Shapiro, I. Large-scale training of foundation models for wearable biosignals. *ICLR '24*, 2024.
- Ahamed, F. and Farid, F. Applying internet of things and machine-learning for personalized healthcare: Issues and challenges. In *iCMLDE '18*, 2018.
- Baldenweg, F., Burger, M., Ratsch, G., and Kuznetsova, R. Multi-modal contrastive learning for online clinical time-series applications. In *ICLR 2024 Workshop on Learning from Time Series For Health*, 2024.
- Cai, H., Gan, C., Wang, T., Zhang, Z., and Han, S. Once for all: Train one network and specialize it for efficient deployment. *ICLR '20*, 2020.
- Chen, W.-Y., Liu, Y.-C., Kira, Z., Wang, Y.-C. F., and Huang, J.-B. A closer look at few-shot classification. In *ICLR '19*, 2019.
- Chen, X. and Yang, J. X-fi: A modality-invariant foundation model for multimodal human sensing. In *ICLR '25*, 2025.
- Chen, Y., Zheng, B., Zhang, Z., Wang, Q., Shen, C., and Zhang, Q. Deep learning on mobile and embedded devices: State-of-the-art, challenges, and future directions. *ACM Comput. Surv.*, 2020.
- Chen, Y., Hu, C., Kimura, T., Li, Q., Liu, S., Wu, F., and Chen, G. Semicmt: Contrastive cross-modal knowledge transfer for iot sensing with semi-paired multi-modal signals. *Proc. ACM Interact. Mob. Wearable Ubiquitous Technol.*, 2024.
- Dhar, S., Guo, J., Liu, J. J., Tripathi, S., Kurup, U., and Shah, M. A survey of on-device machine learning: An algorithms and learning theory perspective. *ACM Trans. Internet Things*, 2021.
- Dhekane, S. G. and Ploetz, T. Transfer learning in human activity recognition: A survey. 2024.
- Eustratiadis, P., Dudziak, Ł., Li, D., and Hospedales, T. Neural fine-tuning search for few-shot learning. *ICLR '24*, 2024.
- Fei-Fei, L., Fergus, R., and Perona, P. Learning generative visual models from few training examples: An incremental bayesian approach tested on 101 object categories. In *2004 Conference on Computer Vision and Pattern Recognition Workshop*, 2004.
- Frankle, J. and Carbin, M. The lottery ticket hypothesis: Finding sparse, trainable neural networks. In *ICLR '19*, 2019.
- Girdhar, R., El-Nouby, A., Liu, Z., Singh, M., Alwala, K. V., Joulin, A., and Misra, I. Imagebind: One embedding space to bind them all. In *CVPR '23*, 2023.
- Gong, T., Kim, Y., Shin, J., and Lee, S.-J. Metasense: Few-shot adaptation to untrained conditions in deep mobile sensing. *SenSys '19*, 2019.
- Guo, P., Hu, B., and Hu, W. Sommelier: Curating dnn models for the masses. *SIGMOD '22*, 2022.
- Gurbuz, S. Z., Rahman, M. M., Kurtoglu, E., Macks, T., and Fioranelli, F. Cross-frequency training with adversarial learning for radar micro-Doppler signature classification (Rising Researcher). In *Radar Sensor Technology XXIV*, 2020.
- Han, R., Zhang, Q., Liu, C. H., Wang, G., Tang, J., and Chen, L. Y. Legodnn: block-grained scaling of deep neural networks for mobile vision. *MobiCom '21*, 2021.
- Hub, P. Discover and publish models to a pre-trained model repository designed for research exploration, 2022.
- Islam, A., Chen, C.-F. R., Panda, R., Karlinsky, L., Radke, R., and Feris, R. A broad study on the transferability of visual representations with contrastive learning. In *ICCV '21*, 2021.
- Jeyakumar, J. V., Lai, L., Suda, N., and Srivastava, M. Sensehar: A robust virtual activity sensor for smartphones and wearables. In *SenSys '19*, 2019.
- Jiang, J., Shu, Y., Wang, J., and Long, M. Transferability in deep learning: A survey. *ArXiv*, 2022.
- Kamboj, A., Nguyen, A. D., and Do, M. N. C3t: Cross-modal transfer through time for sensor-based human activity recognition. 2025.
- Lane, N. D. and Georgiev, P. Can deep learning revolutionize mobile sensing? In *HotMobile '15*, 2015.
- Lee, J., Sattigeri, P., and Wornell, G. Learning new tricks from old dogs: Multi-source transfer learning from pre-trained networks. In *NeurIPS '19*, 2019.
- Leng, Z., Kwon, H., and Ploetz, T. Generating virtual on-body accelerometer data from virtual textual descriptions for human activity recognition. *ISWC '23*, 2023.
- Leng, Z., Bhattacharjee, A., Rajasekhar, H., Zhang, L., Bruda, E., Kwon, H., and Plötz, T. Imugpt 2.0: Language-based cross modality transfer for sensor-based human activity recognition. *Proc. ACM Interact. Mob. Wearable Ubiquitous Technol.*, 2024.
- Li, M., Yumer, E., and Ramanan, D. Budgeted training: Rethinking deep neural network training under resource constraints. 2020.

- Li, Z., Deldari, S., Chen, L., Xue, H., and Salim, F. D. Sensorllm: Aligning large language models with motion sensors for human activity recognition. 2025.
- Liang, H., Zhang, Q., Dai, P., and Lu, J. Boosting the generalization capability in cross-domain few-shot learning via noise-enhanced supervised autoencoder. In *ICCV '21*, 2021.
- Liu, Z., Liu, X., Zhang, J., and Li, K. Opportunities and challenges of wireless human sensing for the smart iot world: A survey. *IEEE Network*, 2019.
- Luo, X., Xu, J., and Xu, Z. Channel importance matters in few-shot image classification. In *ICML '22*, 2022.
- López, O. A. M., López, A. M., and Crossa, J. *Multivariate statistical machine learning methods for genomic prediction*. Springer Nature, 2022.
- Madaan, D., Makino, T., Chopra, S., and Cho, K. Jointly modeling inter- & intra-modality dependencies for multimodal learning. In *NeurIPS '24*, 2024.
- Mastyło, M. Bilinear interpolation theorems and applications. *Journal of Functional Analysis*, 2013.
- mengxi Chen, Zhang, F., Zhao, Z., Yao, J., Zhang, Y., and Wang, Y. Probabilistic conformal distillation for enhancing missing modality robustness. In *NeurIPS '24*, 2024.
- Moon, S., Madotto, A., Lin, Z., Saraf, A., Bearman, A. L., and Damavandi, B. IMU2CLIP: Language-grounded motion sensor translation with multimodal contrastive learning. *EMNLP '23*, 2023.
- Nagrani, A., Chung, J. S., and Zisserman, A. Voxceleb: a large-scale speaker identification dataset. *CoRR*, 2017.
- Nguyen, H. V. and Bai, L. Cosine similarity metric learning for face verification. In *Asian conference on computer vision*, 2010.
- Oh, J., Kim, S., Ho, N., Kim, J.-H., Song, H., and Yun, S.-Y. Understanding cross-domain few-shot learning based on domain similarity and few-shot difficulty. *NeurIPS '22*, 2022.
- Padmanabhan, A., Agarwal, N., Iyer, A., Ananthanarayanan, G., Shu, Y., Karianakis, N., Xu, G. H., and Netravali, R. Gemel: Model merging for Memory-Efficient, Real-Time video analytics at the edge. *NSDI '23*, 2023.
- Polino, A., Pascanu, R., and Alistarh, D. Model compression via distillation and quantization. *ArXiv*, abs/1802.05668, 2018.
- Roggen, D., Calatroni, A., Rossi, M., Holleczeck, T., Förster, K., Tröster, G., Lukowicz, P., Bannach, D., Pirkl, G., Ferscha, A., Doppler, J., Holzmann, C., Kurz, M., Holl, G., Chavarriaga, R., Sagha, H., Bayati, H., Creatura, M., and d. R. Millàn, J. Collecting complex activity datasets in highly rich networked sensor environments. In *INSS'10*, 2010.
- Saenko, K., Kulis, B., Fritz, M., and Darrell, T. Adapting visual category models to new domains. In *Computer Vision–ECCV 2010: 11th European Conference on Computer Vision, Heraklion, Crete, Greece, September 5–11, 2010, Proceedings, Part IV 11*, pp. 213–226. Springer, 2010.
- Sahoo, S., ElAraby, M., Ngnawe, J., Pequignot, Y. B., Precioso, F., and Gagné, C. A layer selection approach to test time adaptation. *AAAI '25*, 2025.
- Schmidt, P., Reiss, A., Duerichen, R., Marberger, C., and Van Laerhoven, K. Introducing wesad, a multimodal dataset for wearable stress and affect detection. *ICMI '18*, 2018.
- Shahapure, K. R. and Nicholas, C. Cluster quality analysis using silhouette score. In *DSAA '20*, 2020.
- Shen, M., Yin, H., Molchanov, P., Mao, L., Liu, J., and Alvarez, J. M. Structural pruning via latency-saliency knapsack. In *NeurIPS '22*, 2022.
- Shi, X., Cao, W., and Raschka, S. Deep neural networks for rank-consistent ordinal regression based on conditional probabilities. 2022.
- Shi, Z., Gu, T., Zhang, Y., and Zhang, X. mmbp: Contact-free millimetre-wave radar based approach to blood pressure measurement. *SenSys '22*, 2023.
- Sobin, C. C. A survey on architecture, protocols and challenges in iot. *Wirel. Pers. Commun.*, 2020.
- Song, X., Huang, K., and Gao, W. Facelistener: Recognizing human facial expressions via acoustic sensing on commodity headphones. In *IPSN '22*, 2022.
- Song, Y., Wang, T., Cai, P., Mondal, S. K., and Sahoo, J. P. A comprehensive survey of few-shot learning: Evolution, applications, challenges, and opportunities. *ACM Comput. Surv.*, 2023.
- Stergiou, G. S., Alpert, B., Mieke, S., and et al. A universal standard for the validation of blood pressure measuring devices: Association for the advancement of medical instrumentation/european society of hypertension/international organization for standardization (aami/esh/iso) collaboration statement. *J Hypertens*, 2018.

- Stisen, A., Blunck, H., Bhattacharya, S., Prentow, T. S., Kjergaard, M. B., Dey, A., Sonne, T., and Jensen, M. M. Smart devices are different: Assessing and mitigating mobile sensing heterogeneities for activity recognition. *SenSys '15*, 2015.
- Szegedy, C., Liu, W., Jia, Y., Sermanet, P., Reed, S., Anguelov, D., Erhan, D., Vanhoucke, V., and Rabinovich, A. Going deeper with convolutions. 2014.
- Tao, R., Zhang, H., Zheng, Y., and Savvides, M. Powering finetuning in few-shot learning: Domain-agnostic bias reduction with selected sampling. *AAAI '22*, 2022.
- Teh, H. Y., Kempa-Liehr, A. W., and Wang, K. I.-K. Sensor data quality: a systematic review. *Journal of Big Data*, 2020.
- Thukral, M., Haresamudram, H., and Plötz, T. Cross-domain har: Few-shot transfer learning for human activity recognition. *ACM Trans. Intell. Syst. Technol.*, 2025.
- Thulasidasan, S., Thapa, S., Dhaubhadel, S., Chennupati, G., Bhattacharya, T., and Bilmes, J. A. An effective baseline for robustness to distributional shift. *CoRR*, 2021.
- Triantafillou, E., Zhu, T., Dumoulin, V., Lamblin, P., Evci, U., Xu, K., Goroshin, R., Gelada, C., Swersky, K., Manzagol, P.-A., and Larochelle, H. Meta-dataset: A dataset of datasets for learning to learn from few examples. In *ICLR '20*, 2020.
- Valpola, H. Chapter 8 - from neural pca to deep unsupervised learning. In *Advances in Independent Component Analysis and Learning Machines*. 2015.
- Venkateswara, H., Eusebio, J., Chakraborty, S., and Panchanathan, S. Deep hashing network for unsupervised domain adaptation. In *Proceedings of the IEEE conference on computer vision and pattern recognition*, pp. 5018–5027, 2017.
- Vinyals, O., Blundell, C., Lillicrap, T., Wierstra, D., et al. Matching networks for one shot learning. *Advances in neural information processing systems*, 29, 2016.
- Wang, W., Li, H., Ding, Z., Nie, F., Chen, J., Dong, X., and Wang, Z. Rethinking maximum mean discrepancy for visual domain adaptation. *IEEE Transactions on Neural Networks and Learning Systems*, 2023.
- Wang, X., Peng, Y., Lu, L., Lu, Z., Bagheri, M., and Summers, R. M. Chestx-ray8: Hospital-scale chest x-ray database and benchmarks on weakly-supervised classification and localization of common thorax diseases. In *CVPR '17*, 2017.
- Wang, Z., Li, J., Wang, W., Dong, Z., Zhang, Q., and Guo, Y. Review of few-shot learning application in csi human sensing. *Artificial Intelligence Review*, 2024.
- Weller, P., Aziz, F., Abdulatif, S., Schneider, U., and Huber, M. F. A mimo radar-based few-shot learning approach for human-id. *EUSIPCO '22*, 2022.
- Wen, H., Li, Y., Zhang, Z., Jiang, S., Ye, X., Ouyang, Y., Zhang, Y., and Liu, Y. Adaptivenet: Post-deployment neural architecture adaptation for diverse edge environments. *MobiCom '23*, 2023.
- Weng, Y., Wu, G., Zheng, T., Yang, Y., and Luo, J. Large model for small data: Foundation model for cross-modal rf human activity recognition. *SenSys '24*, 2024.
- White, C., Safari, M., Sukthanker, R., Ru, B., Elskens, T., Zela, A., Dey, D., and Hutter, F. Neural architecture search: Insights from 1000 papers. 2023.
- Wu, S., Fei, H., Qu, L., Ji, W., and Chua, T.-S. Next-gpt: Any-to-any multimodal llm. *CoRR*, 2023.
- Xiao, J., Li, H., Wu, M., Jin, H., Deen, M. J., and Cao, J. A survey on wireless device-free human sensing: Application scenarios, current solutions, and open issues. *ACM Comput. Surv.*, 2022.
- Xu, D., Mukherjee, S., Liu, X., Dey, D., Wang, W., Zhang, X., Awadallah, A. H., and Gao, J. Few-shot task-agnostic neural architecture search for distilling large language models. In *NeurIPS '22*, 2022.
- Yang, J., Huang, H., Zhou, Y., Chen, X., Xu, Y., Yuan, S., Zou, H., Lu, C. X., and Xie, L. Mm-fi: multi-modal non-intrusive 4d human dataset for versatile wireless sensing. *NeurIPS '23*, 2023.
- Yang, Y., Wan, F., Jiang, Q.-Y., and Xu, Y. Facilitating multimodal classification via dynamically learning modality gap. In *NeurIPS '24*, 2024.
- Yin, G., Zhang, J., Shen, G., and Chen, Y. Fewsense, towards a scalable and cross-domain wi-fi sensing system using few-shot learning. *IEEE Transactions on Mobile Computing*, 2024.
- Yue, X., Zheng, Z., Reed, C., Das, H. P., Keutzer, K., and Sangiovanni-Vincentelli, A. L. Multi-source few-shot domain adaptation. *CoRR*, 2021a.
- Yue, X., Zheng, Z., Zhang, S., Gao, Y., Darrell, T., Keutzer, K., and Sangiovanni-Vincentelli, A. Prototypical cross-domain self-supervised learning for few-shot unsupervised domain adaptation. In *CVPR '21*, 2021b.

- Zhang, J., Xi, R., He, Y., Sun, Y., Guo, X., Wang, W., Na, X., Liu, Y., Shi, Z., and Gu, T. A survey of mmwave-based human sensing: Technology, platforms and applications. *IEEE Communications Surveys & Tutorials*, 2023a.
- Zhang, W., Deng, L., Zhang, L., and Wu, D. A survey on negative transfer. *IEEE/CAA Journal of Automatica Sinica*, 2023b.
- Zhang, X., Zhang, Y., Shi, Z., and Gu, T. *mmFER: Millimetre-wave Radar based Facial Expression Recognition for Multimedia IoT Applications*. MobiCom '23. 2023c.
- Zhang, Y., Gu, T., and Zhang, X. Mddroidlite: a release-and-inhibit control approach to resource-efficient deep neural networks on mobile devices. In *SenSys '20*, 2020.
- Zhang, Y., Gu, T., and Zhang, X. Mddroid: A chainsgd-reduce approach to mobile deep learning for personal mobile sensing. *IEEE/ACM Trans. Netw.*, 2022.
- Zhao, A., Ding, M., Lu, Z., Xiang, T., Niu, Y., Guan, J., and Wen, J.-R. Domain-adaptive few-shot learning. In *WACV '21*, 2021.
- Zhao, M., Li, T., Abu Alsheikh, M., Tian, Y., Zhao, H., Torralba, A., and Katabi, D. Through-wall human pose estimation using radio signals. In *CVPR '18*, 2018.
- Zhao, S., Wang, G., Zhang, S., Gu, Y., Li, Y., Song, Z., Xu, P., Hu, R., Chai, H., and Keutzer, K. Multi-source distilling domain adaptation. In *AAAI '20*, 2020.
- Zhou, K., Yang, Y., Qiao, Y., and Xiang, T. Domain adaptive ensemble learning. *IEEE Transactions on Image Processing*, 2021.
- Zhou, T., Niu, P., Wang, X., Sun, L., and Jin, R. One fits all: Power general time series analysis by pretrained LM. *NeurIPS '23*, 2023.

## Appendix

The appendix is organized as follows:

- Section A illustrates more details on our experiment setup, including implementation details, developed real-world sensing applications, experimental setups, dataset statistics, evaluation metrics, and computation resources we used for our experiments.
- Section B introduces additional technique details of different components in XTransfer.
- Section C gives more experimental results about ablation study and benchmarking.

### A. Experiment setup details

#### A.1. Settings for learning with few data

A typical FSL method consists of two stages—meta-training and meta-testing (Chen et al., 2019). In meta-training stage, FSL requires a large-scale source dataset from the same modality (*i.e.*, typically specific to the application) to train source models from scratch. The source dataset is divided into a support set and a query set<sup>1</sup>. Data for each set is loaded according to the  $n$ -way (*i.e.*, number of classes) and  $n$ -shot (*i.e.*, number of samples per class) format (Song et al., 2023). The meta-testing stage follows the same structure but uses unseen target data. Specifically, the target support set is used to *adapt* the source models, which are then evaluated on the target query set. Leave-One-Out Cross-Validation (LOOCV) is widely used as the *de facto* standard for evaluating datasets involving multiple users in human sensing (Gong et al., 2019). LOOCV works by leaving one user out as the target for meta-testing while using the remaining users to train the source models during meta-training in each round. The MetaSense (Gong et al., 2019) is used as an oracle baseline under FSL settings, where sufficient target sensing datasets are provided during meta-training stage. Unlike FSL, cross-domain FSL focuses primarily on meta-testing and transfers pre-trained source models across domains (*i.e.*, different users), while remaining within the same modality (Oh et al., 2022). In this work, the cross-modality FSL settings are defined similarly to cross-domain FSL, but extend it to transferring pre-trained source models across different modalities, using only few labeled target data and without assuming any additional unlabeled target data.

#### A.2. Setups in preliminary study

As shown in Figure 1(a), we test a standard *overfitting* metric, defined as  $\frac{|Accuracy_{train} - Accuracy_{test}|}{Accuracy_{train}}$  (López et al., 2022). In Figure 1(b), we apply a standard cross-domain FSL benchmarking (Oh et al., 2022) to gain insights. It uses Earth Mover’s Distance (EMD) to measure similarity between source models and targets. We test 3 source models (using a pre-trained ResNet18 from PyTorch Hub (Hub, 2022)) from 3 modalities, *e.g.*, miniImageNet (Image), Newsgroup (Text), and OPPORTUNITY (Sensing), shown in Table 2. We also use 5 sensing datasets (HHAR, WESAD, Writing, Emotion, and Gesture) as targets, and employ 2 well-known image datasets (CUB and ChestX) as reference targets to the Image, detailed in Table 2. It also assesses FSL difficulty by fine-tuning source models on targets under 5-shot settings with LOOCV enabled. Since source models usually involve a large number of classes (*e.g.*, 100 classes in miniImageNet), we propose a class pairing strategy that pairs source and target classes exhibiting similar latent feature distributions across modalities.

#### A.3. Setups in layer-wise analysis

In Section 3, we conduct a layer-wise analysis to gain insights into cross-modality model transfer with few sensor data. To set up, we continue to use the standard ResNet18 (Hub, 2022) and segment it as 9 L-Blocks, as shown in Table 3. We also employ the default reshaping (see Section B.1) on HHAR as target with 5-shot setting, and use the original source model input (miniImageNet) as reference, marked as Original. We examine the single-source baselines, including Transfer Learning (TL) (Jiang et al., 2022), Fine-tuning (FT) (Oh et al., 2022), MAML (Chen et al., 2019), DAPN (Zhao et al., 2021), and MetaSense (Gong et al., 2019) as the oracle baseline, shown in Table 1. To precisely track the MMC shift changes at each layer during fine-tuning,

<sup>1</sup>The support set and query set are assumed to be drawn from the same data distribution (Triantafillou et al., 2020).

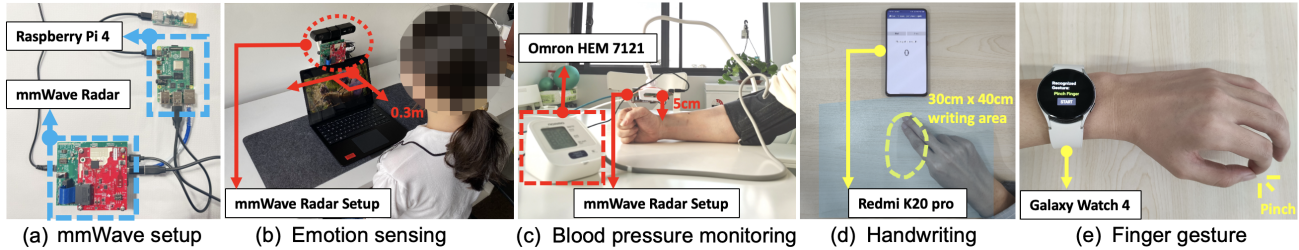


Figure 5. (a) Embedded mmWave radar testbed setup; (b)-(e) Built human sensing applications across different real-world settings.

#### A.4. Layer-wise metric

To precisely track the MMC shift changes at each layer during fine-tuning, we essentially use the Silhouette score (S-score) (Shahapure & Nicholas, 2020) as the layer-wise metric to evaluate how well the features are being fine-tuned. The S-score is in the range from -1 to 1 and being better if closing to 1. To verify whether the S-score indicates the layer performance, we observe the changes in the S-score and accuracy at each layer using the TL (Jiang et al., 2022) and Original methods. Figure 6(a) also shows that S-score and accuracy by Original are positively correlated, converging in a layer-wise manner. TL’s S-score also performs equivalently to its accuracy (*i.e.*, S-score drop along with accuracy drop) in detecting the negative transfer across different layers.

#### A.5. Implementation

We implement XTransfer using PyTorch version 1.4.0. We also benchmark XTransfer with a full development cycle of cross-modality FSL tasks, including pre- and post-processing, training, and inference on commercial edge devices. Once pre-trained source models and few sensor data are processed in the cloud via XTransfer, compact models can be seamlessly converted to various DL platforms (*e.g.*, PyTorch Mobile, TFLite) for broader edge deployments. To enable reproducibility of the results, we fix all random seeds in the code, set the evaluation mode consistently when evaluating output models, and enable CUDA convolution determinism. To measure model resource overhead (*e.g.*, FLOPs and parameters), we use the standard PyTorch OpCounter. For regression tasks, class-based transformation (Shi et al., 2022) enables compatibility.

#### A.6. Developed sensing applications

To evaluate XTransfer on real-world human sensing targets, we essentially develop 4 human sensing applications, as shown in Figure 5. These include: (1) emotion recognition via facial expressions (*i.e.*, Emotion) and (2) non-contact blood pressure monitoring (*i.e.*, BP) based on an embedded mmWave radar setup, (3) handwriting tracking (*i.e.*, Writing) using ultrasound based on a smartphone, and (4) gesture recognition (*i.e.*, Gesture) using IMU and PPG sensors based on a smartwatch. The data collection is approved with ethics approval and involves 40 subjects. The corresponding target sensing datasets are shown in Table 2 with detailed specifications.

#### A.7. Hardware setup and computation environment

We evaluate XTransfer on real-world testbeds using 3 commercial edge devices, ranging from smartwatch to Raspberry Pi (Table 5). For example, Figure 5(a) presents an embedded mmWave radar setup which consists of a TI IWR1843Boost and a Raspberry Pi 4 using ROS Melodic on Ubuntu 18.04.4. In addition, we implement both smartwatch and smartphone testbeds using PyTorch Android version 1.10.0. We also employ servers equipped with NVIDIA GeForce RTX 3090 GPU to build our cloud environment.

#### A.8. Training details

In the Repair stage, we fine-tune the generative transfer module (see Section 4) for 100 episodes using SGD with a learning rate of  $1e-2$  and momentum 0.95. We apply a step-based learning rate scheduler with a step size of 20 and a decay factor of 0.5. We also use standard early stopping with a patience of 20. We retain the training parameters of the baselines in Table 1 as specified in their original implementations.

Device	ROM	RAM	CPU	Battery	OS
Galaxy Watch 4	16GB	1.5GB	Exynos W920	247mAh	Wear OS 3.5
Raspberry Pi 4	64GB	8GB	Broadcom BCM2711	-	Ubuntu 18.04.4
Redmi K20 Pro	128GB	8GB	Snapdragon 855	4000mAh	Android 11

Table 5. Edge devices specification.

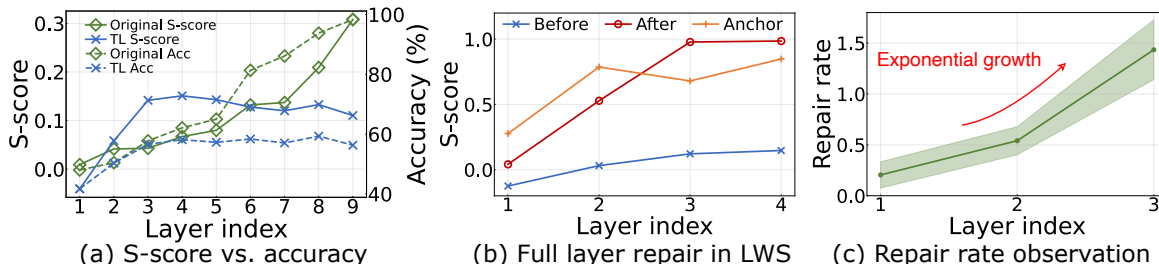


Figure 6. Design insights. (a) shows layer-wise metric correlation. (b)(c) present efficient search insights into LWS control using multiple source models.

## B. Technical details

### B.1. Default reshaping

To align with source model input shape, we develop a *default reshaping* to transform sensor data shape. It uses bilinear interpolation (Mastyło, 2013) (*i.e.*, Resizer) to resize the height and width, and a fixed convolutional layer (*i.e.*, Fixed header) with a  $1 \times 1$  kernel to match the input channels (Szegedy et al., 2014), placed between source models and sensor data.

### B.2. PCA-based layer channel removal

In the Removal stage, layer channel removal is designed to further enhance layer-wise performance while optimizing resource usage. This is achieved by removing unnecessary layer channels at each layer. Existing pruning techniques (Shen et al., 2022; Frankle & Carbin, 2019) typically rely on layer channel importance metrics, such as the L2 norm, calculated from MMC. However, due to MMC shift, these metrics may inaccurately assess layer channel importance, resulting in degraded layer performance. To address this, we propose using PCA-based layer channel importance, derived from the optimized component weights during the repair process, as a more reliable metric for layer channel removal. Our objective is to remove unnecessary layer channels  $\tilde{ch}$  while preserving the maximum S-score ( $Score(\cdot)$ ), formulated as  $\arg \max_{(\tilde{ch} \in CH)} Score(PCA(MMC(ft_{ij}^r), \tilde{ch}), Y_t)$ , where  $CH$  denotes the set of all layer channels,  $r$  denotes the repaired latent features  $ft_{ij}$ , and  $Y_t$  denotes the target labels.

### B.3. Setups for efficient search insights

To gain design insights of efficient search for LWS control (see Section 5), we observe a complete process where all layers are repaired using the HHAR dataset and a Multi-ResNet18 model (*i.e.*, 5 source models with 45 L-unit), as shown in Table 3. Figure 6(b) shows the changes in the S-score across three states: after pairing anchors (*i.e.*, Anchor), before and after applying the SRR pipeline (*i.e.*, Before and After, respectively), in a layer-wise manner. The results show that the SRR pipeline successfully increases the S-score from Before state (*i.e.*, lower bound) to align with the Anchor state (*i.e.*, the objective). This indicates a strong correlation between the After state’s S-score and both Before and Anchor values. These insights lead to the observation for designing the repair rate growth model.

### B.4. Observation for designing repair rate growth model

Our key idea is to estimate the repaired S-score (*i.e.*, repair value) of each layer *before* initiating SRR processing, allowing us to decide whether to bypass unnecessary repairs. To empirically examine this, we first define a repair rate function to capture this correlation as  $rate_n = (After - Before)/Anchor = (V_{ij}^n - Score(Pro(ft_{ij}^n), Y_t))/Score(Pro(fs_{ij}^n), Y_s)$ , where  $Y_s$  denotes the source labels, and we normalize  $rate_n \in [0, 1]$ . We then repeat the process multiple times to observe the changes in  $rate_n$ . Figure 6(c) shows that the repair rate demonstrates *exponential growth*. Thus, we design the repair rate growth model based on an exponential growth model (see Section 5.2).

Epoch (#)	#1	#20	#40	#60	#80	#100
With Alignment	0.486	0.355	0.350	0.339	0.333	0.331
Without Alignment	0.476	0.406	0.393	0.383	0.378	0.387

Table 6. Feature space alignment performance across training epochs.

PCA Variation	3-shot		5-shot		10-shot	
	Accuracy (%)	Time (mins)	Accuracy (%)	Time (mins)	Accuracy (%)	Time (mins)
Standard PCA-#2	58.96	3.9	71.85	5.6	80.74	10.3
Sparse PCA-#2	58.52	3.8	64.67	5.3	75.11	8.8

Table 7. Impact of PCA variations on accuracy and training time.

### B.5. Post fine-tuning

After LWS control is completed, we add either a linear classifier or a regression layer (*e.g.*, a fully connected layer) at the end of the model to finalize its backbone. To strengthen layer-wise dependence, we perform a quick post fine-tuning process, updating only the connectors and fully connected layers.

## C. Additional experiment results

### C.1. Feature space alignment performance

In the process of feature space alignment (Section 4.1), we use a standard Hungarian algorithm based on default distance metrics to select and pair classes. To verify its effectiveness, we keep using the setup of HHAR, the standard pre-trained ResNet18 on miniImageNet, and the standard PCA under 5-shot settings to examine how our repair loss performs with/without the feature space alignment, especially in the initial layer repairing. Repairing the initial layer is critical, as it often introduces a large, disorganized feature space and significantly affects the repair of subsequent layers. In Table 6, the results show that with the alignment, the repair loss decreases considerably faster by 1.87 times on average, compared to the case without alignment. This indicates that the design of feature space alignment notably contributes to the repairing process.

### C.2. Impact of PCA variations

Since our method uses the repair learning mechanism that relies on backpropagation (BP) through the reduced-orthogonal feature space, standard PCA can project data into a linear subspace and maintain a closed-form, differentiable structure, which enables smooth integration with BP in our end-to-end learning pipeline. Compared to advanced choices such as kernel PCA, we find that it introduces a non-linear mapping into a high-dimensional feature space using a kernel function, and its projections are generally not differentiable with respect to input features. This makes it incompatible with our pipeline. To test whether linear PCA variations affect the overall performance of XTransfer, we compare standard PCA against sparse PCA using the setup of HHAR based on the ResNet18 under 3 few-shot settings with a default search depth of 3. As shown in Table 7 (#2 denotes 2-component setting), sparse PCA reduces learning time slightly by 11.6% on average, but suffers from a notable accuracy drop by 4.4% on average. These results support the choice of standard PCA as a balanced and practical solution.

### C.3. Impact of PCA components

We then evaluate the impact of PCA components on the model accuracy and time efficiency of XTransfer. Since the feature space with different dimensionalities adjusted by PCA components may impact our method performance, we test 3 different levels of PCA components, including PCA-#2 (top two components), PCA-80% (selected components covering 80% of the feature variance), and PCA-Max (maximum components available). We continue to use the same setup as above with the standard PCA. The results in Table 8 show that as the number of PCA components increases, the training time rises notably. In fact, PCA-Max results in an average accuracy drop of 4.5% compared to PCA-80%. By contrast, PCA-#2 achieves the best accuracy-to-time ratio across all n-shot settings, with competitive accuracy and the lowest training time, hence we use PCA-#2 as the default throughout the evaluation.

PCA Components	3-shot		5-shot		10-shot	
	Accuracy (%)	Time (mins)	Accuracy (%)	Time (mins)	Accuracy (%)	Time (mins)
PCA-#2	58.96	3.9	71.85	5.6	80.74	10.3
PCA-80%	63.61	5.2	74.72	7.6	80.00	12.9
PCA-Max	60.00	7.2	75.56	8.1	70.28	16.9

Table 8. Impact of PCA components on accuracy and training time.

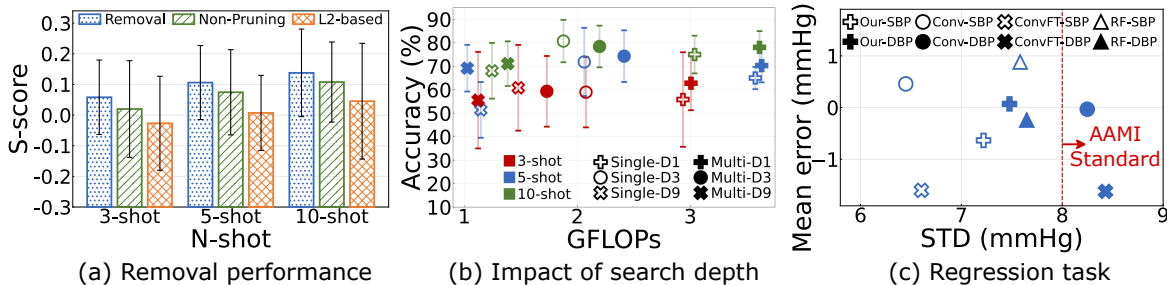


Figure 7. Ablation study evaluating the performance of components, search parameters, and applications.

Alignment Method	3-shot		5-shot		10-shot	
	Accuracy (%)	ATR	Accuracy (%)	ATR	Accuracy (%)	ATR
<b>MMD Loss (Wang et al., 2023)</b>	55.78	1.63	65.89	2.01	68.52	1.83
<b>Repair Loss</b>	65.11	2.33	69.33	2.45	72.07	2.29
<b>PCA + Repair Loss</b>	58.96	1.42	71.85	1.56	80.74	2.09

Table 9. Comparison of non-linear feature alignment methods across n-shot settings.

#### C.4. Non-linear feature alignment performance

We essentially use PCA to construct a fixed, orthogonal anchor feature space in which alignment is measured and the anchor-based repair loss is computed at each layer across modalities. The proposed connector (*i.e.*, repair generator) dynamically maps target-modality features into this anchor space, enabling the non-linear feature alignment. To examine the impact of using a linear PCA anchor space and to compare the alignment performance, we evaluate our repair loss with and without PCA against a Maximum Mean Discrepancy (MMD) loss baseline (Wang et al., 2023). To set up, we keep using the standard ResNet18 on miniImageNet (Table 3) as sources on HHAR as target (Table 2) in 3-, 5- and 10-shot settings with all configurations identical except for the alignment loss. As shown in Table 9, our repair loss with PCA anchor space achieves the highest accuracy of 70.5% and the lowest ATR of 1.69 on average across all n-shot settings. Compared to our repair loss without PCA, MMD loss performs a lower accuracy on average. This indicates that MMD loss is limited to aligning the latent feature distribution when the feature space is highly complex due to strong cross-modality discrepancies and only few target data. In addition, adversarial alignment methods such as DAPN (Zhao et al., 2021) and MDDA (Zhao et al., 2020) also face similar difficulties under these conditions, as shown in Tables 4 and 12. Moreover, the PCA anchor space provides a more stable basis for alignment and consistently enhances our repair loss performance. As a result, these findings further validate the effectiveness of our method in cross-modality FSL settings.

#### C.5. Layer-wise convergence comparison

To further examine layer-wise convergence across the above alignment methods, we observe the feature alignment process in the initial layer. To normalize heterogeneous losses, we follow the strategy in (Li et al., 2020) and compute the loss descent (LD) relative to the initial loss, enabling a fair comparison of convergence rates across different loss functions (*i.e.*, how much each loss decreases from its starting point), defined as  $LD(t) = (L(0) - L(t)) / L(0) \times 100\%$ , where  $t$  denotes the epoch index. All experimental settings remain the same as in the previous setup. As shown in Table 10, our repair loss with the PCA anchor achieves the largest loss descent of 28.87%, which is 1.79 and 1.87 times faster than the repair loss without PCA and the MMD loss, respectively. Interestingly, MMD loss presents a large initial drop but quickly plateaus, while our repair loss starts more gradually and accelerates over training. In contrast, the PCA-based repair maintains a steady and consistent descent across epochs, highlighting the benefits of aligning features in a fixed, orthogonal anchor space. These findings further support that our method provides both effective feature alignment and practical training efficiency, consistent with the efficiency study in Section C.10.

Epoch (#)	#10	#20	#30	#40	#50	#60	#70	#80	#90	#100
MMD Loss (Wang et al., 2023)	6.46%	10.0%	11.63%	12.81%	13.5%	14.3%	14.66%	14.98%	15.27%	15.41%
Repair Loss	0.03%	1.67%	2.66%	4.93%	5.26%	7.16%	8.06%	10.4%	14.66%	16.14%
PCA + Repair Loss	5.12%	13.45%	16.54%	19.23%	20.55%	21.3%	25.96%	26.21%	27.6%	28.87%

Table 10. Comparison of layer-wise convergence rates across alignment methods.

Backbone	Accuracy (%)	FLOPs (G)
Multi-Conv4	65.56	0.01
Multi-ResNet10	63.61	0.14
Multi-ResNet18	78.44	2.19

Table 11. Performance of different source model backbones in terms of accuracy and FLOPs.

### C.6. Removal performance

We next evaluate how layer channel removal enhances the average S-score of selected layers. We continue to use the same setup as above under 5-shot settings. We employ L2 norm-based (*i.e.*, L2-based) model pruning (Frankle & Carbin, 2019; Shen et al., 2022) as the baseline and compare it with the setting where layer channel removal is disabled (*i.e.*, Non-Pruning). Figure 7(a) demonstrates that the proposed layer channel removal outperforms both Non-Pruning and L2-based pruning across all settings, achieving an average S-score of 0.1 by selected layers. L2-based pruning achieves a lower average S-score than Non-Pruning, indicating that the layer channel importance may be inaccurately estimated, resulting in degraded performance. These results show that the proposed layer channel removal further improves layer performance by accurately removing unnecessary layer channels at each layer.

### C.7. Impact of search depth

In this experiment, we investigate how different search depths affect the accuracy and resource overhead (*e.g.*, FLOPs) of output models. Varying the search depth alters the search window sizes with the number of layer candidates, which can lead to different output model backbones and accuracy. To quantify these differences, we employ HHAR as target, ResNet18 on miniImageNet (Single) and Multi-ResNet18 (Multi) on 5 image datasets as sources (shown in Table 2) in 3-, 5- and 10-shot settings. We also utilize MetaSense in Table 1 as the oracle baseline. Both Single and Multi models have up to 9 L-unit, hence we set three different search depths as D1, D3, D9. Figure 7(b) shows that the output models of both Single-D1 and Multi-D1 result in high FLOPs, while that of both Single-D9 and Multi-D9 achieve low FLOPs. As search depth decreases, the search process becomes longer, and it triggers LWS control to make more decisions on recombining layers, which results in a suboptimal model backbone with high FLOPs. Although both Single-D3 and Multi-D3 do not produce the lowest FLOPs on average, they outperform others and achieve the highest average model accuracy of 70.52% and 70.69%, respectively, across the three settings. Therefore, we set D3 as the default search depth, as it provides the best balance between resource overhead and accuracy of the output models.

### C.8. Impact of model backbones

The current implementation of XTransfer uses homogeneous pre-trained source models. Technically, the layer-wise repairing and recombination techniques impose no fundamental restrictions on the choice of model backbone and work with various architectural variants. To verify this, we evaluate the trade-off between accuracy and computational cost using different source backbones. We continue to use HHAR, and test Multi-Conv4, Multi-ResNet10, and Multi-ResNet18 in a 5-shot, multi-source setting shown in Table 3. The results in Table 11 demonstrate that the average accuracy declined, transitioning from Multi-Conv4 to Multi-ResNet10, and then increasing with Multi-ResNet18. Interestingly, Multi-Conv4, despite having fewer parameters, outperforms Multi-ResNet10, which may be attributed to differences in model quality or distributional divergence between source and target. Multi-ResNet18, though with higher FLOPs, achieves the best accuracy. It suggests that larger models trained on large-scale cross-modality datasets exhibit superior latent features, which notably contribute to such model transfer. Our techniques such as the connectors are designed to flexibly handle the layers with different shapes/structures, and can be extended to heterogeneous model backbones. In addition, our method focuses on latent feature alignment rather than specific feature extraction. It remains fully compatible with advanced source models (*e.g.*, with temporal encoders), which can be seamlessly integrated into our pipelines with minimal or no modifications.

## XTransfer: Modality-Agnostic Few-Shot Model Transfer for Human Sensing at the Edge

Method	HHAR			WESAD			Gesture			Writing			Emotion			ChestX		
	3-shot	5-shot	10-shot															
ProtoNet (Chen et al., 2019)	0.51	0.46	0.50	0.44	0.49	0.52	0.51	0.56	0.59	0.69	0.79	0.73	0.51	0.49	0.55	0.22	0.23	0.25
DAPN (Zhao et al., 2021)	0.49	0.51	0.55	0.57	0.61	0.63	0.46	0.49	0.51	0.75	0.79	0.80	0.48	0.50	0.59	0.24	0.24	0.26
MAML (Chen et al., 2019)	0.37	0.42	0.42	0.40	0.58	0.66	0.37	0.41	0.39	0.32	0.40	0.35	0.22	0.27	0.31	0.22	0.20	0.22
SemiCMT (Chen et al., 2024)	0.33	0.39	0.49	0.37	0.40	0.44	0.24	0.34	0.43	0.27	0.39	0.48	0.24	0.34	0.47	0.25	0.26	0.28
GPT2 (Zhou et al., 2023)	0.11	0.09	0.12	0.13	0.09	0.09	0.13	0.14	0.17	0.14	0.19	0.20	-	-	-	-	-	-
<b>Our-Single</b>	<b>1.42</b>	<b>1.57</b>	<b>2.09</b>	<b>2.76</b>	<b>2.61</b>	<b>2.51</b>	<b>1.55</b>	<b>1.90</b>	<b>1.76</b>	<b>2.11</b>	<b>1.88</b>	<b>1.84</b>	<b>0.82</b>	<b>1.07</b>	<b>1.26</b>	<b>0.83</b>	<b>1.04</b>	<b>1.24</b>
MDDA (Zhao et al., 2020)	0.03	0.04	0.04	0.08	0.08	0.08	0.02	0.03	0.03	0.03	0.02	0.02	0.03	0.03	0.03	0.04	0.04	0.04
MCW (Lee et al., 2019)	0.06	0.05	0.05	0.06	0.07	0.06	0.04	0.05	0.05	0.06	0.06	0.06	0.05	0.05	0.05	0.04	0.04	0.05
<b>Our-Multi</b>	<b>1.71</b>	<b>1.47</b>	<b>1.64</b>	<b>3.00</b>	<b>2.70</b>	<b>2.75</b>	<b>1.20</b>	<b>1.25</b>	<b>1.63</b>	<b>1.93</b>	<b>1.96</b>	<b>1.53</b>	<b>0.96</b>	<b>1.23</b>	<b>1.73</b>	<b>0.68</b>	<b>1.24</b>	<b>0.83</b>

Table 12. Comparison in ATR ratio. Top-2 results are highlighted in **bold**

Method	HHAR (mins)			WESAD (mins)			Gesture (mins)			Writing (mins)			Emotion (mins)			ChestX (mins)		
	3-shot	5-shot	10-shot	3-shot	5-shot	10-shot	3-shot	5-shot	10-shot	3-shot	5-shot	10-shot	3-shot	5-shot	10-shot	3-shot	5-shot	10-shot
DAPN (Zhao et al., 2021)	2.38	4.62	11.78	1.49	2.54	6.78	3.36	6.12	15.72	4.12	7.71	20.97	2.99	7.34	18.86	2.14	4.57	12.04
MAML (Chen et al., 2019)	124.28	125.66	183.20	71.71	77.07	115.87	118.79	129.79	191.95	165.06	129.27	194.36	94.81	98.40	153.20	66.20	72.17	106.97
SemiCMT (Chen et al., 2024)	3.02	8.27	10.23	1.82	2.48	5.63	4.81	9.42	12.83	10.10	13.92	18.75	3.39	7.32	11.48	2.84	5.28	8.33
<b>Our-Single</b>	3.98	5.57	7.95	2.12	2.99	4.33	5.64	7.80	11.24	7.94	10.54	14.69	5.58	7.43	9.88	3.65	4.75	6.84
<b>Our-Multi</b>	9.25	15.33	15.25	4.40	5.38	7.21	12.49	15.12	24.37	15.35	17.36	32.38	11.72	13.39	19.75	8.41	9.33	13.61

Table 13. Comparison in training time of each method.

Method	HHAR (%)			WESAD (%)			Gesture (%)			Writing (%)			Emotion (%)			ChestX (%)		
	3-shot	5-shot	10-shot															
DAPN (Zhao et al., 2021)	48.85	49.19	51.79	44.62	49.49	48.81	42.73	48.71	50.59	43.88	56.63	57.51	44.67	59.73	63.12	46.66	47.32	48.48
MAML (Chen et al., 2019)	59.59	79.32	89.72	52.58	70.27	77.52	53.11	66.75	73.21	72.56	85.47	92.22	63.39	72.78	75.01	44.52	55.46	61.36
SemiCMT (Chen et al., 2024)	55.60	73.43	78.91	38.83	50.33	67.89	57.02	72.16	98.04	75.14	79.12	81.79	60.30	63.43	68.60	41.54	50.05	63.43
<b>Our-Single</b>	<b>18.27</b>	<b>18.90</b>	<b>19.48</b>	<b>15.95</b>	<b>16.46</b>	<b>16.98</b>	<b>20.67</b>	<b>21.71</b>	<b>22.51</b>	<b>19.92</b>	<b>20.67</b>	<b>21.08</b>	<b>18.24</b>	<b>19.20</b>	<b>19.96</b>	<b>16.97</b>	<b>17.58</b>	<b>18.80</b>
<b>Our-Multi</b>	<b>18.31</b>	<b>20.77</b>	<b>22.06</b>	<b>18.00</b>	<b>19.42</b>	<b>23.10</b>	<b>20.49</b>	<b>22.49</b>	<b>24.49</b>	<b>18.68</b>	<b>19.25</b>	<b>21.69</b>	<b>16.45</b>	<b>18.18</b>	<b>19.85</b>	<b>15.33</b>	<b>17.69</b>	<b>19.62</b>

Table 14. Comparison in GPU utilization of each method during training. Top-2 results are highlighted in **bold**

### C.9. Regression task performance

We also evaluate the effectiveness of XTransfer in a regression task using the BP dataset, which includes both systolic (SBP) and diastolic (DBP) sensor data shown in Table 2 collected by the blood pressure monitoring application. We employ the pre-trained ResNet18 on miniImageNet as the source model and use the 5-shot setting. To integrate this into the SRR pipeline, we transform the regression task by treating individual regression labels as distinct classes for anchor class pairing. For benchmarking, we use mean error (ME) and standard deviation (STD), following the Advancement of Medical Instrumentation (AAMI) standard, which accepts an ME within 5 mmHg and STD within 8 mmHg (Stergiou et al., 2018). We employ a random forest (RF) based method (Shi et al., 2023) as the oracle baseline. Besides, we train a Conv4 backbone in Table 3 (Conv) using LOOCV, and the fine-tuned Conv (ConvFT) as the baselines. Figure 7(c) shows that both XTransfer and the RF methods surpass the AAMI standard. In particular, XTransfer outperforms the baselines and RF in estimating both SBP (ME: -0.64mmHg, STD: 7.2mmHg) and DBP (ME: 0.07mmHg, STD: 7.47mmHg) tasks. These results demonstrate that XTransfer is highly efficient in handling regression tasks with few sensor data.

### C.10. Training efficiency

To test the practical training efficiency in the cloud, we further evaluate training time across the selected baselines. We use the same experimental setups as in Table 14, Section 6.3. For MAML (Chen et al., 2019) and SemiCMT (Chen et al., 2024), which require model re-training from pre-trained source models to adapt to the target modality classes, training time includes both re-training and fine-tuning. For DAPN (Zhao et al., 2021), it reflects model adaptation process on few target data. The results in Table 13 show that both Our-Single and Our-Multi achieve significant training time reductions compared to MAML. Our-Single also matches or exceeds DAPN and SemiCMT in training efficiency. Notably, even when using up to 5 source models, Our-Multi remains practical training efficiency, requiring only 2.05 times more training time on average compared to Our-Single across all datasets and shot settings. This further supports the practicability and scalability of our method.

Dataset	Type	FLOPs	Params	Watch		Pi		Phone	
				Latency (ms)	Mem (MB)	Latency (ms)	Mem (MB)	Latency (ms)	Mem (MB)
HHAR	Single	1.51G	0.75M	625.5	125.5	274.18	246.62	26.86	179.5
	Multi	1.46G	2.16M	634.5	140	249.26	247.83	28.34	209
WESAD	Single	1.19G	0.74M	604.5	120	240.05	244.64	25.77	168
	Multi	0.89G	0.34M	460.5	122	209.52	235.55	21.57	181
Gesture	Single	1.21G	2.25M	706.5	135	259.25	251.26	31.5	192
	Multi	1.45G	2.09M	692	137	268.79	253.7	30.96	190
Writing	Single	1.32G	0.87M	467.5	126	261.71	242.33	29.79	183.5
	Multi	1.28G	0.73M	513	124.5	285.2	247.01	34.67	185
Emotion	Single	1.51G	0.49M	767.5	130.5	390.36	271.02	41.1	171.5
	Multi	1.43G	2.14M	781	142	285.16	251.48	37.9	189.5
ChestX	Single	0.64G	0.72M	690.5	126	210.45	237.45	29.57	165
	Multi	1.06G	0.7M	670	130.5	261.14	236.96	30.14	183.5
ResNet18	-	3.67G	11.18M	1060	189	703.52	303.75	89.8	311
Multi-ResNet18	-	14.68G	55.9M	5816	356	4242.27	482.26	454.44	436

Table 15. On-device Performance.

### C.11. Training resource usage

We then examine the training resource usage of XTransfer by measuring GPU utilization (Util) in the cloud. We focus on the above baselines that require model re-training or adaptation for transfer, *e.g.*, MAML (Chen et al., 2019), DAPN (Zhao et al., 2021), and SemiCMT (Chen et al., 2024), excluding methods that rely solely on fine-tuning or distance-based techniques. The experimental setup remains the same as above. As shown in Table 14, both our methods achieve the lowest GPU Util across all n-shot settings compared to baselines. Notably, both Our-Single and Our-Multi achieve a substantial reduction in GPU Util by 2.6 to 3.6 times and 2.5 to 3.5 times on average, respectively, compared to baselines. This is due to our layer-wise method, which progressively repairs and recombines only a subset of layers rather than training the entire model at once. It also highlights the effectiveness of our compact connector design. Despite leveraging multiple source models, Our-Multi shows no significant increase (*e.g.*, only 3.67%) in training resource usage, further highlighting its efficiency and scalability. Hence, XTransfer significantly reduces cloud resource usage, enabling scalable model transfer.

### C.12. On-device performance

We now evaluate the on-device performance of deploying XTransfer’s output models on 3 commercial edge devices (Table 5), focusing on resource overhead metrics such as FLOPs, parameters, latency per call, and peak memory footprint. For each target dataset, we test both types of output models created by our single-source (Single) and multi-source (Multi) methods. We also use ResNet18 and Multi-ResNet18 (Table 3) as baselines. As shown in Table 15, all output models achieve significant reductions in model resource overhead, *e.g.*, FLOPs is reduced by 2.4 to 5.7× for Single models and by 10.1 to 16.5× for Multi models, compared to the baselines. These recombined models also demonstrate substantial improvement in on-device performance. Specifically, in the Single method, latency is reduced by 1.4 to 4.1 × and peak memory footprint decreases by 1.8 to 3.9×. In the Multi method, the reductions are even more pronounced, with latency dropping by 7.4 to 21× and memory footprint by 2.2 to 8.4×, compared to the baselines. These results prove that XTransfer successfully achieves streamlined edge deployment.